

# UniChange: Unifying Change Detection with Multimodal Large Language Model

Xu Zhang<sup>1\*</sup>Danyang Li<sup>2\*</sup>Xiaohang Dong<sup>1</sup>Tianhao Wu<sup>4</sup>Hualong Yu<sup>1</sup>Jianye Wang<sup>1</sup>Qicheng Li<sup>1†</sup>Xiang Li<sup>2,3</sup><sup>1</sup>TMCC, Computer Science, Nankai University<sup>2</sup>VCIP, Computer Science, Nankai University<sup>3</sup>NKIARI, Futian, Shenzhen<sup>4</sup>CMEC, Sichuan Agricultural University

{xu\_zhang, danyang.li}@mail.nankai.edu.cn, liqicheng@nankai.edu.cn

## Abstract

Change detection (CD) is a fundamental task for monitoring and analyzing land cover dynamics. While recent high performance models and high quality datasets have significantly advanced the field, a critical limitation persists. Current models typically acquire limited knowledge from single-type annotated data and cannot concurrently leverage diverse binary change detection (BCD) and semantic change detection (SCD) datasets. This constraint leads to poor generalization and limited versatility. The recent advancements in Multimodal Large Language Models (MLLMs) introduce new possibilities for a unified CD framework. We leverage the language priors and unification capabilities of MLLMs to develop UniChange, the first MLLM-based unified change detection model. UniChange integrates generative language abilities with specialized CD functionalities. Our model successfully unifies both BCD and SCD tasks through the introduction of three special tokens: [T1], [T2], and [CHANGE]. Furthermore, UniChange utilizes text prompts to guide the identification of change categories, eliminating the reliance on predefined classification heads. This design allows UniChange to effectively acquire knowledge from multi-source datasets, even when their class definitions conflict. Experiments on four public benchmarks (WHU-CD, S2Looking, LEVIR-CD+, and SECOND) demonstrate SOTA performance, achieving IoU scores of 90.41, 53.04, 78.87, and 57.62, respectively, surpassing all previous methods. The code is available at <https://github.com/Erxucombeon/UniChange>.

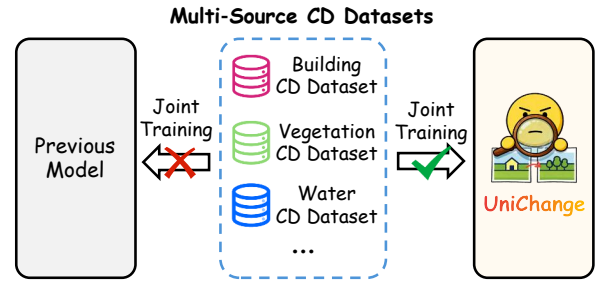


Figure 1. Inconsistency in multi-source change detection datasets.

## 1. Introduction

Change Detection (CD) is the process of observing and analyzing multi-temporal remote sensing images to identify changes in land surface cover. It serves as a fundamental task in the remote sensing field and a cornerstone of modern geospatial analysis. Change detection plays a vital role in numerous applications, ranging from sustainable urban planning [41] and natural disaster assessment [51] to ecological monitoring [38] and land resource management [1]. Depending on the required level of detail, CD tasks are typically categorized into two primary sub-domains: Binary Change Detection (BCD) and Semantic Change Detection (SCD). BCD, the simpler task, primarily identifies the locations where change has occurred, but may focus on a single object of interest or not specify the nature of these transformations. While useful for automated monitoring, it provides relatively coarse-grained information. In contrast, SCD is a more complex and refined task. It not only determines the location of change but also identifies the “from-to” semantic transition [31] (e.g., from “forest” to “urban land”). This granular understanding of semantic shifts offers richer insights, providing more robust decision support for the aforementioned applications.

In the deep learning era, methods such as FCNN [9]

\*Equal Contribution

†Corresponding Author

and IFN [46] establish the Siamese Network architecture as the dominant paradigm for BCD. Subsequent research shifted focus toward enhancing the fusion and interaction of dual-temporal features. BiT [4] inserts interaction modules between the encoder and decoder to fuse dual-temporal features. Concurrently, Transformer-based architectures [2, 17, 43, 47] are proposed to extract and fuse these features at various stages within the encoder. Changer [16] pioneer a dual-temporal feature exchange paradigm by inserting a series of feature interaction layers directly within the feature extractor. Furthermore, recent works like SAM-CD [12] have begun to adapt Vision Foundation Models (VFs) [25, 35, 50] for the BCD task. However, a fundamental limitation of these methods is the necessity of training a specialized model for each individual dataset. RSBuilding [40] partially mitigate this issue by leveraging a VFM, enabling joint training on multiple building datasets for both building extraction and change detection. However, its framework is essentially tailored to building-related tasks and cannot be extended to other categories of land cover change.

Compared to BCD, SCD is considered a more challenging task. Its core complexity lies in the fact that SCD must not only localise changes but also identify specific “from-to” semantic transitions between land cover categories. To address this challenge, the early HRSCD [10] adopt a decoupling strategy, jointly training semantic segmentation and binary change detection, which is subsequently refined by MTSCD-Net [7]. Subsequent studies have turned to deeper feature interaction and temporal modelling. Bi-SRNet [11] improves semantic change detection via bi-temporal reasoning and consistency modeling. Furthermore, SCD-SAM [31] leverages the representational capabilities of VFs and designs a refined dual-encoder and dual-decoder architecture. Therefore, the specificity and complexity of the SCD task requires the design of a specialised architecture, which objectively hinders its harmonisation with the BCD task in terms of model architecture.

By analyzing the previous BCD and SCD methods, we have identified two problems that have persisted in the field. The first is dataset incompatibility. As shown in Fig. 1, a positive sample in one dataset (e.g., ‘building’) may be explicitly defined as a negative background sample in another dataset (e.g., ‘vegetation’). This semantic conflict prevents traditional models from being jointly trained on such multi-source data. Secondly, the different requirements of BCD and SCD lead to incompatible model architectures, as shown in Fig. 2(a) and Fig. 2(b). This has led to a proliferation of highly specialized models, each with limited knowledge from a single annotation type of data (BCD or SCD). This mutually independent design approach results in poor model generalization and severely limits the versatility of the CD system in practical applications.

To address the fundamental challenges within the change

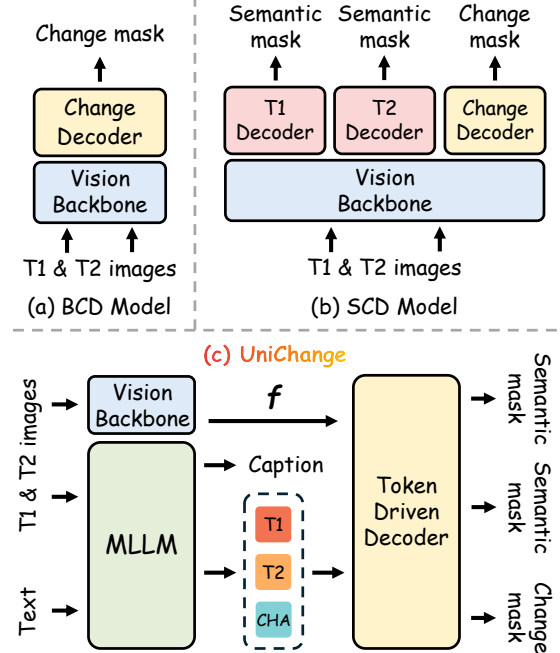


Figure 2. Inconsistency in model architecture.

detection domain, we propose UniChange. UniChange is a unified change detection model based on multimodal large language models. Not only does UniChange simultaneously support both BCD and SCD tasks, but it also enables joint training using multi-source datasets. The architecture of UniChange is shown in Fig. 2(c). We introduce three special tokens [T1], [T2], and [CHANGE] to enable the model to handle both BCD and SCD tasks concurrently. Furthermore, UniChange leverages textual cues to guide change region classification, thereby eliminating the reliance on pre-defined classification heads found in traditional approaches. This design facilitates the extraction of unified knowledge from diverse, multi-source change detection datasets, even when semantic category conflicts exist between datasets. Overall, our contributions are as follows:

- We propose UniChange, the first unified framework for change detection based on MLLM. It is designed to simultaneously accommodate both Binary Change Detection (BCD) and Semantic Change Detection (SCD) tasks within a single end-to-end model, whilst enabling training using multi-source change detection datasets.
- We introduce a Token Driven Decoder strategy. The strategy incorporates three special tokens into MLLM: [T1], [T2] and [CHANGE]. It enables the model to be trained simultaneously on change detection tasks and the semantic understanding of dual-temporal images.
- Comprehensive experiments demonstrate that UniChange achieves state-of-the-art performance, significantly outperforming previous methods on both the BCD and SCD benchmark datasets.

## 2. Related Work

### 2.1. Change Detection

The field of Change Detection (CD) is broadly divided into two sub-fields: Binary Change Detection (BCD) and the more complex Semantic Change Detection (SCD). The latter is more challenging as it requires identifying the "from-to" semantic information, not just the presence of change.

Early deep learning methods for BCD are dominated by CNN-based architectures. FCNN [9] is one of the early methods to utilize the paradigm of comparing features from two weight-sharing encoders. IFN [46] extends this by adding deep supervision and attention mechanisms. To better model global context, Transformer-based methods are introduced, including BiT [4], ChangeFormer [2], Swin-SUNet [47] and Changer [16]. Other notable works, such as DMINet [17], and HATNet [43], further explore hybrid architectures and deep feature interaction. More recently, VFM-based methods have emerged. SAM-CD [12] focuses on adapting VFM [25, 35, 50] to the BCD task, while RS-Building [40] leverages VFM to unify building-specific extraction and change detection tasks. These methods are difficult to jointly train on diverse and multi-class change detection datasets, and their generalization ability is limited.

Compared with BCD task, SCD task is more complex. HRSCD [10] and MTSCD-Net [7] utilize multi-task frameworks with separate branches for semantic segmentation and binary change detection. SCDNet [32] employs siamese networks and further utilizes attention mechanisms to refine multi-scale difference features, and Bi-SRNet [11] proposes cross-temporal semantic reasoning blocks to enhance feature consistency. Most recently, VFM-based adaptation emerges, with SCD-SAM [31] adapting VFM by designing a specialized dual-encoder and dual-decoder system specifically for the SCD task. The differences between BCD and SCD task lead to inconsistency between their model architectures, resulting in poor versatility.

### 2.2. Multimodal Large Language Model

Initial MLLMs, such as LLaVA [29], MiniGPT-4 [53], and InstructBLIP [8], focus on tasks such as image captioning and visual question answering (VQA). Subsequent research has further developed this capability, enabling it to support refined visual understanding, perception and generation at both regional and pixel levels [27, 28, 33, 42, 45, 49]. While transformative, their application to remote sensing (RS) has been challenging. RS-specific MLLMs such as RSGPT [23], GeoChat [26], and GeoPixel [36] have emerged, but these largely focus on single-image interpretation. This architectural's focus on single images makes them ill-suited for comparative, bi-temporal analysis, leaving a significant gap in their ability to perform pixel-level grounding for change detection.

## 3. Method

In this section, we first define the unified change detection task involving dual-temporal remote sensing images and textual queries, as presented in Sec. 3.1. This is followed by a detailed presentation of the UniChange architecture in Sec. 3.2, which integrates the Multimodal Large Language Model (MLMM) for instruction grounding and the Change-Perception Vision Module for pixel-level segmentation. Finally, we detail the training strategy in Sec. 3.3, including the unified loss functions designed to manage both binary and semantic constraints.

### 3.1. Task Definition

We define the task of unified change detection as follows. Let the input consist of a pair of dual-temporal remote sensing images,  $x_{img1}, x_{img2} \in R^{H \times W \times C}$ , captured at times  $T_1$  and  $T_2$ , where  $H$ ,  $W$ , and  $C$  represent the height, width, and channel dimensions, respectively. An accompanying text input,  $x_{txt}$ , provides the change query instruction. This instruction can range from a general binary query (e.g., "Please segment all regions that have changed.") to a fine-grained semantic query (e.g., "Please segment the semantic masks of the changed regions."). The core goal is to generate a set of masks ( $\hat{M}$ ) that accurately adhere to the semantic instructions provided by the query  $x_{txt}$ . This overall process can be formulated as:

$$\hat{M} = \Phi_{UniChange}(x_{img1}, x_{img2}, x_{txt}), \quad (1)$$

where  $\Phi_{UniChange}$  represents the entire unified change detection model.

### 3.2. Architecture

**Embedding as Change.** Current Change Detection (CD) models suffer from two fundamental problems: dataset incompatibility due to semantic conflicts across different sources, and architectural divergence between specialized Binary Change Detection (BCD) and Semantic Change Detection (SCD) tasks. This fragmentation prevents joint training, leading to poor generalization and limited versatility. Therefore, we propose UniChange. This framework implements our proposed "embedding-as-change" paradigm, which integrates generative language abilities with specialized CD functionalities, thereby achieving a true unification of multi-source datasets and multi-tasks. The pipeline of our method is illustrated in Fig. 3(a). We utilize the MLLM to encode the dual-temporal remote sensing images  $x_{img1}, x_{img2}$  and the textual query  $x_{txt}$  into a unified multimodal representation. To unify both binary and semantic change detection within a single framework, we introduce three specialized tokens into the MLLM's vocabulary: [CHANGE], [T1], and [T2]. Guided by the textual query  $x_{txt}$ , the MLLM then performs autoregressive generation,

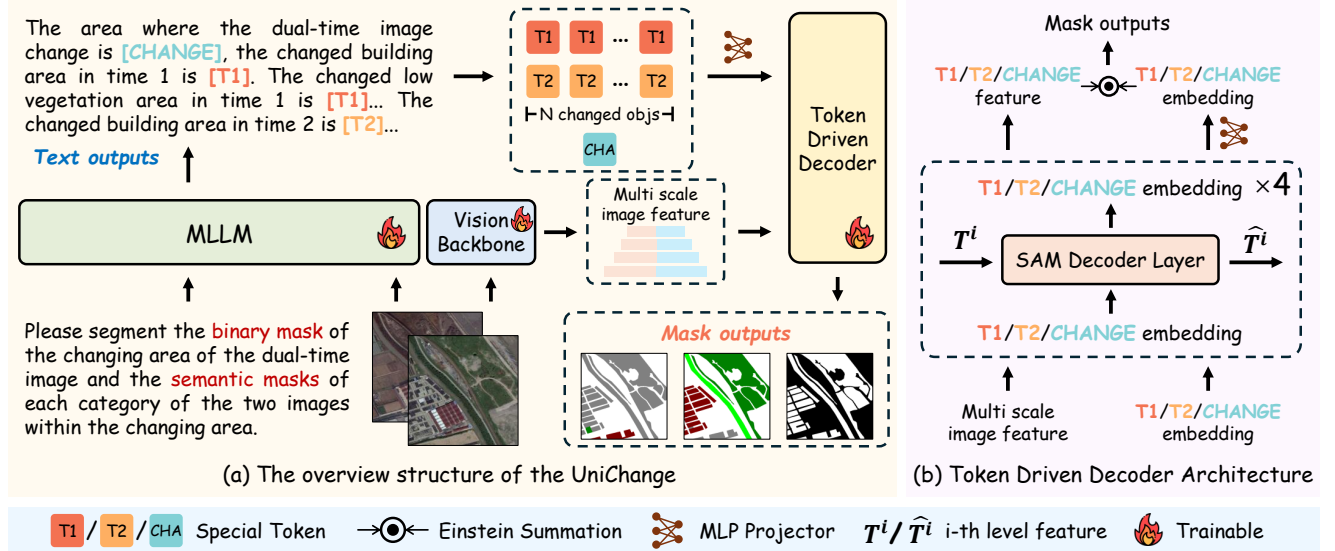


Figure 3. The overview structure of UniChange is shown in (a). UniChange generates text outputs based on text instructions and dual-temporal remote sensing images. The text outputs incorporate a series of special tokens ([T1], [T2], and [CHANGE]). Concurrently, the dual-temporal remote sensing images undergo feature extraction via the Vision Backbone. These features, alongside the embeddings corresponding to the special tokens, are fed into the Token-Driven Decoder. Ultimately, UniChange generates the masks corresponding to the text instructions. The overall structure of the Token-Driven Decoder is shown in (b). It receives dual-temporal remote sensing image features and special token embeddings, generating corresponding masks.

producing a response sequence  $y_{txt}$  that strategically places these tokens based on the specific task query. This process can be formulated as:

$$y_{txt} = \mathcal{F}_{MLLM}(x_{img1}, x_{img2}, x_{txt}), \quad (2)$$

where  $\mathcal{F}_{MLLM}$  represents the MLLM's generation function. When the MLLM intends to generate instructions for a specific change mask (e.g., the binary change mask or a semantic mask for  $T_1$ ), its output  $y_{txt}$  includes the corresponding special token (e.g., [CHANGE] or [T1]). Subsequently, we extract the final-layer hidden state embedding  $h_{task}$  corresponding to the position of the task-specific token ([CHANGE], [T1], or [T2]) within  $y_{txt}$ . This raw embedding is then projected into the feature space compatible with the downstream vision module using a dedicated  $MLP(\cdot)$  layer:

$$\hat{h}_{task} = MLP(h_{task}), \quad (3)$$

these projected sparse embeddings  $\hat{h}_{task}$  serve as the dynamic, instruction-guided queries.

Concurrently, the vision backbone  $\mathcal{F}_{enc}$  first extracts base dense visual features from the dual-temporal remote sensing images. It then employs a feature pyramid, constructed using max-pooling and transposed convolutional layers, to generate four levels of multi-scale representations for each temporal image. This results in two multi-scale feature sets, denoted as  $\{F_1^i\}$  and  $\{F_2^i\}$ , where  $i \in \{1, 2, 3, 4\}$ .

Finally, these dual-temporal visual features, along with the projected task embeddings  $\hat{h}_{task}$ , are fed into the token driven decoder  $\mathcal{F}_{dec}$  to generate the final mask  $\hat{M}_{task}$ . The entire process can be described as:

$$\begin{aligned} \{F_1^i\}, \{F_2^i\} &= \mathcal{F}_{enc}(x_{img1}, x_{img2}), \\ \hat{M}_{task} &= \mathcal{F}_{dec}(\{F_1^i\}, \{F_2^i\}, \hat{h}_{task}). \end{aligned} \quad (4)$$

We employ a hybrid fine-tuning strategy: parameter-efficient fine-tuning (PEFT) using LoRA [22] is applied only to the MLLM's language decoder, while all other components of the model are fully fine-tuned.

**Token Driven Decoder.** The token driven decoder,  $\mathcal{F}_{dec}$ , is specifically architected to bridge the MLLM's high-level instructions and the pixel-level requirements of the change detection task. Its architecture is illustrated in Fig. 3(b). This decoder processes the visual features conditioned by the task-specific query embeddings derived from the MLLM. Specifically, the projected embeddings  $\{\hat{h}_{t1}, \hat{h}_{t2}, \hat{h}_{change}\}$  (obtained from Eq. (3)) serve as the initial task queries. Let  $E^0$  represent the concatenation of these initial queries:

$$E^0 = \Phi_{Cat}(\hat{h}_{t1}, \hat{h}_{t2}, \hat{h}_{change}), \quad (5)$$

the concatenated query embeddings  $E^0$  are then hierarchically refined through four decoders. Each decoder  $i$  processes its corresponding multi-scale visual features  $F_1^i$  and  $F_2^i$  by first adding a learnable positional encoding ( $PE$ ),

flattening ( $\Phi_{Flat}$ ) them into token sequences, and concatenating ( $\Phi_{Cat}$ ) them into a unified visual sequence  $T^i$ :

$$T^i = \Phi_{Cat}(\Phi_{Flat}(F_1^i + PE), \Phi_{Flat}(F_2^i + PE)). \quad (6)$$

A dual cross-attention mechanism then refines both the task queries and the visual sequence. The task queries  $E^{i-1}$  (from the previous level) first attend to themselves ( $\mathcal{A}_{self}$ ), then attend to the visual sequence  $T^i$  ( $\mathcal{A}_{cross}$ ), and are subsequently processed by an FFN ( $\mathcal{F}_{FFN}$ ). Concurrently, the visual sequence  $\hat{T}^i$  is also updated by attending to these newly refined task queries. This recursive process is defined as:

$$\begin{aligned} E^i &= \mathcal{F}_{FFN}(\mathcal{A}_{cross}(\mathcal{A}_{self}(E^{i-1}), T^i)), \\ \hat{T}^i &= \mathcal{A}_{cross}(T^i, E^i), \end{aligned} \quad (7)$$

the refined queries  $E^4$  from the final level, along with the refined visual sequences  $\hat{T}^i$  from all levels, are used for the final mask generation.

First, we process the refined visual sequences  $\hat{T}^i$  (where  $i \in \{1, 2, 3, 4\}$ ) from each decoder level. As shown in Eq. (8), the sequence  $\hat{T}^i$  from each level is split and reshaped ( $\Phi_{Split/Reshape}$ ) back into its corresponding 2D dual-temporal feature maps,  $\hat{F}_1^i$  and  $\hat{F}_2^i$ :

$$\{\hat{F}_1^i\}, \{\hat{F}_2^i\} = \Phi_{Split/Reshape}(\{\hat{T}^i\}). \quad (8)$$

These multi-level features are then individually upsampled ( $\Phi_{Up}$ ) to a uniform scale and concatenated ( $\Phi_{Cat}$ ) along the channel dimension. A fusion module ( $\Phi_{fuse}$ ) integrates them to create two final dense representations,  $F_{t1}$  and  $F_{t2}$ . The dense change feature map,  $F_{change}$ , is then derived by element-wise subtraction:

$$\begin{aligned} F_{t1} &= \Phi_{fuse}(\Phi_{Cat}(\{\Phi_{Up}(\hat{F}_1^i)\})), \\ F_{t2} &= \Phi_{fuse}(\Phi_{Cat}(\{\Phi_{Up}(\hat{F}_2^i)\})), \\ F_{change} &= F_{t1} - F_{t2}. \end{aligned} \quad (9)$$

The refined query embeddings  $E^4$  from the final decoder level are then processed. These embeddings are first projected ( $\Phi_{proj}$ ) and then split ( $\Phi_{Split}$ ) into the individual task representations  $\hat{e}_{t1}$ ,  $\hat{e}_{t2}$ , and  $\hat{e}_{change}$ . These projected embeddings are used to filter their corresponding dense feature maps ( $F_{t1}$ ,  $F_{t2}$ ,  $F_{change}$ ) to generate the final masks:

$$\begin{aligned} \hat{e}_{t1}, \hat{e}_{t2}, \hat{e}_{change} &= \Phi_{Split}(\Phi_{proj}(E^4)), \\ \hat{M}_{task} &= \mathcal{M}_{gen}(F_{task}, \hat{e}_{task}), \\ \text{task} &\in \{t1, t2, change\} \end{aligned} \quad (10)$$

where  $\mathcal{M}_{gen}$  represents the mask generation function, which performs Einstein summation. This unified structure allows UniChange to flexibly generate the corresponding masks based on the user's instructions.

### 3.3. Training Strategy

Our method is trained end-to-end to jointly optimize UniChange. The overall objective function,  $\mathcal{L}_{total}$ , is defined as a weighted summation of all contributing loss terms:

$$\mathcal{L}_{total} = \lambda_{txt} \mathcal{L}_{txt} + \mathcal{L}_{mask}, \quad (11)$$

the comprehensive mask loss,  $\mathcal{L}_{mask}$ , is designed to enforce pixel-level accuracy across the unified change detection task and is defined as the summation of four distinct components:

$$\mathcal{L}_{mask} = \lambda_{BCE} \mathcal{L}_{BCE} + \lambda_{Dice} \mathcal{L}_{Dice} + \lambda_{SS} \mathcal{L}_{SS} + \lambda_{CS} \mathcal{L}_{CS}, \quad (12)$$

in Eq. (12),  $\lambda_{txt}$ ,  $\lambda_{BCE}$ ,  $\lambda_{Dice}$ ,  $\lambda_{SS}$ , and  $\lambda_{CS}$  serve as the weighting coefficients for the text generation loss, Binary Cross-Entropy loss, Dice loss, Semantic Segmentation loss, and Change Similarity loss, respectively.  $\mathcal{L}_{txt}$  is the standard autoregressive Cross-Entropy Loss applied to the LMM's generated sequence.  $\mathcal{L}_{BCE}$  is the Binary Cross-Entropy Loss, which optimizes the model's prediction confidence by penalizing differences between the predicted probability map and the binary ground truth at the pixel level.  $\mathcal{L}_{Dice}$  is the Dice Loss, which focuses on evaluating the overlap between the predicted mask and the ground truth mask. It is particularly effective for mitigating the influence of class imbalance inherent in change detection tasks.  $\mathcal{L}_{SS}$  is the 2D Cross-Entropy Loss for semantic segmentation, which computes pixel-wise classification errors across all spatial locations in the dual-temporal predictions, thereby penalizing misclassification across all semantic categories.  $\mathcal{L}_{CS}$  is the Change Similarity Loss, which employs cosine embedding to constrain the semantic feature representations across the two time points, encouraging similarity in unchanged areas and divergence in changed areas.

Crucially, during training on BCD datasets, the semantic constraint losses,  $\mathcal{L}_{SS}$  and  $\mathcal{L}_{CS}$ , are set to zero. They are only computed when training on fully annotated SCD datasets. By optimizing this comprehensive objective function, UniChange ensures effective alignment between linguistic instructions and pixel-level perception, simultaneously achieving accuracy in both binary and multi-class semantic change detection.

## 4. Experiments

### 4.1. Experimental Setting

We employ LLaVA-7B-v1-1 [29] as the base MLMM. For the Change-Perception Vision Module, we adopt the RSBuilding-ViT-L [40] backbone, which is a SAM backbone structure pre-trained on remote sensing imagery.

We adopt 4 NVIDIA 80G H100 GPUs for training, and the training scripts leverage the deepspeed [34] engine. We

utilize the AdamW [30] optimizer and set the base learning rate to  $5 \times 10^{-5}$ . We set the batch size per device to 1 and the gradient accumulation step to 8. We train the model for 10 epochs, and each epoch consists of 400 training steps.

The comprehensive loss function, which was introduced in Sec. 3.3, utilizes several weighting coefficients to balance its multiple objective components. Specifically, we set the MLMM’s text generation loss weight  $\lambda_{txt}$  to 1.0. The mask loss components are weighted with  $\lambda_{BCE}$  set to 2.0,  $\lambda_{Dice}$  set to 0.5,  $\lambda_{SS}$  set to 0.5, and  $\lambda_{CS}$  set to 1.0.

## 4.2. Datasets

**BCD Datasets.** We evaluate the Binary Change Detection (BCD) capability of UniChange on three widely adopted remote sensing datasets: WHU-CD [24], LEVIR-CD+ [3], and S2Looking [37]. The WHU-CD dataset consists of a pair of large dual-temporal remote sensing images with a resolution of 0.075 m/pixel, each with a size of  $32507 \times 15354$  pixels. For standardized evaluation, we crop these large images into  $1024 \times 1024$  patches. We then split these patches into training, validation, and test sets following an 8:1:1 ratio. The LEVIR-CD+ dataset is an extended version of LEVIR-CD, offering 985 pairs of  $1024 \times 1024$  images primarily focusing on building changes. We utilize the original  $1024 \times 1024$  image size for training and testing on this dataset, which provides 637 training patches and 348 testing patches. Finally, the S2Looking dataset provides a total of 5000 image pairs captured from side-looking rural areas globally, featuring a resolution of 0.5 to 0.8 m/pixel and containing over 65920 annotated change instances. These image pairs are divided into 3500 for training, 1000 for testing and 500 for validation. These datasets collectively allow for robust assessment across different resolutions and geographic regions.

**SCD datasets.** We evaluate the Semantic Change Detection (SCD) capabilities of UniChange on the SECOND dataset [44]. This dataset is specifically designed to support fine-grained change analysis, requiring models to simultaneously pinpoint the location of changes and classify the semantic category transitions. The dataset comprises 4662 pairs of dual-temporal remote sensing images with a  $512 \times 512$  resolution, featuring a ground sampling distance ranging from 0.3 m to 0.5 m. It covers six detailed land-cover categories: buildings, low vegetation, trees, water, playgrounds, and bare ground. The predominance of unchanged pixels in the dataset creates a significant class imbalance, which places higher demands on the model’s generalization capability.

## 4.3. Evaluation Metrics

**BCD Metrics.** To evaluate the performance of UniChange on the BCD task, we employ four standard pixel-level metrics: Precision (P), Recall (R), F1 Score (F1), and Intersec-

tion over Union (IoU). Precision measures the proportion of correctly predicted change pixels among all pixels classified as change. Recall indicates the proportion of true positive pixels among all truly positive pixels in the ground truth. The F1 Score is the harmonic mean of Precision and Recall, providing a single metric that balances these two measures. Finally, IoU measures the overlap between predicted and ground-truth positive regions, serving as a robust measure of segmentation quality.

The metrics are individually defined as follows, where TP, TN, FP, and FN represent the number of true positive pixels, true negative pixels, false positive pixels, and false negative pixels, respectively:

$$\begin{aligned} P &= \text{TP} / (\text{TP} + \text{FP}), \\ R &= \text{TP} / (\text{TP} + \text{FN}), \\ \text{F1} &= 2 \times P \times R / (P + R), \\ \text{IoU} &= \text{TP} / (\text{TP} + \text{FP} + \text{FN}). \end{aligned} \quad (13)$$

**SCD Metrics.** The assessment of SCD model performance is executed using a collection of specialized metrics, all derived from the confusion matrix  $Q = q_{ij}$ , where  $q_{ij}$  records the count of pixels classified as class  $i$  with a ground truth label of  $j$ .

The mean Intersection over Union for SCD (mIoU) is utilized to evaluate overall segmentation quality, established as the arithmetic mean of the Intersection over Union for the regions without change ( $\text{IoU}_{nc}$ ) and all changing regions ( $\text{IoU}_c$ ):

$$\text{mIoU} = (\text{IoU}_{nc} + \text{IoU}_c) / 2, \quad (14)$$

the term  $\text{IoU}_{nc}$  measures the overlap between the predicted unchanged regions and the ground-truth unchanged regions:

$$\text{IoU}_{nc} = q_{00} / (\sum_{i=0}^N q_{i0} + \sum_{j=0}^N q_{0j} - q_{00}), \quad (15)$$

conversely,  $\text{IoU}_c$  measures the overall segmentation quality of all change regions, treating all distinct semantic change categories as a single change class:

$$\text{IoU}_c = \sum_{i=1}^N \sum_{j=1}^N q_{ij} / (\sum_{i=0}^N \sum_{j=0}^N q_{ij} - q_{00}). \quad (16)$$

The Separation kappa coefficient (SeK) provides a valuable measure of semantic discrimination amidst class imbalance, particularly designed to diminish the influence of the prevalent unchanged class. SeK is computed from the confusion matrix  $Q = q_{ij}$ , where  $\hat{q}_{ij} = q_{ij}$ , but  $\hat{q}_{00} = 0$ ,

Table 1. Comparison with existing sota methods on WHU-CD, S2Looking and LEVIR-CD+.

Methods	WHU-CD				S2Looking				LEVIR-CD+			
	P	R	F1	IoU	P	R	F1	IoU	P	R	F1	IoU
FC-Siam-diff [9]	48.84	88.96	63.06	46.05	<b>83.49</b>	32.32	46.60	30.38	80.88	77.65	79.23	65.60
DASNet [5]	83.77	91.02	87.24	77.37	45.06	48.71	47.29	30.97	77.51	78.03	77.77	63.63
SNUNet [15]	91.28	87.25	89.22	80.54	45.25	50.60	47.78	31.39	78.90	78.23	78.56	64.69
BIT [4]	91.56	87.84	89.66	81.26	70.26	56.53	62.65	45.61	82.37	79.73	81.03	68.11
ChangeFormer [2]	91.76	84.85	88.17	78.85	70.73	49.25	58.07	40.91	84.29	80.81	82.51	70.23
RFL-CDNet [18]	91.33	91.46	91.39	84.15	65.72	60.82	63.17	46.17	79.95	84.04	81.94	69.41
SAM-CD [12]	<b>96.87</b>	85.67	90.92	83.35	72.80	58.92	65.13	48.29	79.71	81.35	81.96	69.43
Meta-CD [20]	89.00	90.35	89.67	81.27	74.08	54.00	62.47	45.42	80.17	84.13	82.10	69.93
SA-CDNet [19]	95.29	93.67	94.47	89.52	81.28	56.24	66.48	49.79	85.55	83.44	84.43	73.06
ChangeCLIP [14]	96.02	93.58	94.78	90.08	-	-	-	-	<b>88.46</b>	83.90	86.12	75.63
SFCD-Net [48]	95.42	93.14	94.27	89.16	72.60	61.70	66.71	50.05	87.25	85.65	86.44	76.12
TPP [6]	96.05	92.76	94.37	89.34	73.51	62.19	67.38	50.80	85.81	84.36	85.08	74.03
<b>UniChange</b>	95.83	<b>94.11</b>	<b>94.96</b>	<b>90.41</b>	73.48	<b>65.60</b>	<b>69.32</b>	<b>53.04</b>	87.88	<b>88.49</b>	<b>88.19</b>	<b>78.87</b>

and is calculated as:

$$\rho = \sum_{i=0}^N \hat{q}_{ii} / \sum_{i=0}^N \sum_{j=0}^N \hat{q}_{ij},$$

$$\eta = \sum_{i=0}^N \left( \sum_{j=0}^N \hat{q}_{ij} \times \sum_{j=0}^N \hat{q}_{ji} \right) / \left( \sum_{i=0}^N \sum_{j=0}^N \hat{q}_{ij} \right)^2, \quad (17)$$

$$SeK = e^{IoU_c - 1} \cdot (\rho - \eta) / (1 - \eta).$$

The performance of UniChange on the SCD task is comprehensively evaluated using BCD metrics (IoU and F1) and SCD metrics (mIoU and SeK).

#### 4.4. Results

**BCD Results.** As shown in Tab. 1, UniChange achieves the best F1 score and IoU score across all three evaluated benchmarks: WHU-CD, S2Looking, and LEVIR-CD+. On the WHU-CD dataset, our method achieves a top F1 score of 94.96 and an IoU score of 90.41. On the S2Looking dataset, our method obtains an F1 score of 69.32 and an IoU score of 53.04, exceeding the TPP result (67.38 F1 score, 50.80 IoU score). Furthermore, on the LEVIR-CD+ dataset, our approach demonstrates superior performance, setting a new SOTA F1 score of 88.19 and IoU score of 78.87, outperforming the second-best model, SFCD-Net (86.44 F1 score, 76.12 IoU score). The ability to achieve consistently superior F1 score and IoU score across these diverse benchmarks highlights the effectiveness and broad applicability of UniChange.

**SCD Results.** As shown in Tab. 2, UniChange achieves the best performance across all key metrics on the SEC-OND dataset. UniChange achieves the highest IoU score of 57.62 and the top mIoU score of 72.85, confirming its

Table 2. Comparison with existing sota methods on SECOND.

Methods	IoU	mIoU	F1	SeK
HRSCD.Str3 [9]	44.52	63.57	61.61	8.89
HRSCD.Str4 [9]	53.34	69.44	69.57	15.97
SCDNet [32]	-	70.78	-	17.23
ChangeMask [52]	52.17	69.67	68.57	14.75
SAAN [21]	53.49	-	-	18.03
BiSRNet [11]	55.99	72.38	71.79	19.64
DFINet [39]	-	72.61	-	20.12
MLFA-Net [13]	56.33	72.45	72.06	20.11
MTSCD-Net [7]	55.84	71.68	71.67	20.57
SAM-SCD [31]	56.82	71.92	72.46	20.60
<b>UniChange</b>	<b>57.62</b>	<b>72.85</b>	<b>73.12</b>	<b>23.02</b>

superior capability in accurately delineating the overall regions of change and non-change. Furthermore, the model sets the SOTA F1 score at 73.12, surpassing SAM-SCD (72.46). Most notably, on the highly rigorous SeK metric, which provides a robust measure of overall semantic accuracy and inter-class differentiation, our approach obtains the highest value of 23.02, outperforming the next best performance from SAM-SCD (20.60). This comprehensive superiority across all metrics confirms that UniChange’s architecture is highly effective for handling the challenging task of multi-class change detection.

#### 4.5. Ablation Study

In this section, we aim to validate the efficacy of the proposed components and strategies by conducting a series of ablation experiments. Unless otherwise specified, we employ LLaVA-7B-v1-1 as the MLMM and RSBuilding-ViT-L as our vision backbone. Furthermore, semantic supervi-

Table 3. Effects of dual-temporal image semantic supervision.

Semantic Supervision		WHU-CD			
T <sub>1</sub>	T <sub>2</sub>	P	R	F1	IoU
-	-	95.38	93.51	94.42	89.46
✓	-	95.77	93.45	94.59	89.74
-	✓	95.16	<b>94.39</b>	94.77	90.06
✓	✓	<b>95.83</b>	94.11	<b>94.96</b>	<b>90.41</b>

sion is applied to the dual-temporal remote sensing images within the WHU-CD dataset. The lora rank is set to 8, lora alpha is consistently set to twice the lora rank.

**Effects of dual-temporal images Semantic Supervision.** The WHU-CD dataset provides comprehensive annotations, offering not only the standard change mask but also individual semantic segmentation masks for each of the dual-temporal remote sensing images (T<sub>1</sub> and T<sub>2</sub>). To validate the effects of this dual-temporal semantic supervision, we conducted an ablation study categorizing experiments into four groups. As shown in Tab. 3, The optimal performance is realized by the final group, which applied semantic supervision to both temporal images (T<sub>1</sub> and T<sub>2</sub>). The intermediate configurations (supervising only T<sub>1</sub> or T<sub>2</sub>) achieve progressive performance improvements over the baseline (which lacks semantic supervision), but are outperformed by the fully supervised setting. This monotonic trend confirms the synergistic effect of dual-temporal semantic supervision in enhancing feature discrimination, thereby affirming its efficacy for the change detection task within our unified framework.

**Effects of Different Vision Backbone.** To validate the effects of different vision backbones on performance, we conduct a series of experiments as shown in Tab. 4. We test three distinct encoders (SAM, SAM2, and RSBuilding-ViT-L) under two configurations: a frozen setting and a fine-tuned (ft) setting. The SAM and RSBuilding backbones have the exact same architecture, differing only in their pre-trained weights. The experimental results reveal two clear trends. First, the fine-tuned group’s overall performance is superior to the frozen group’s across both datasets. Second, RSBuilding-ViT-L delivers the highest performance within both the fine-tuned and frozen groups.

**Effects of Lora Rank.** To validate the effects of different LoRA ranks on model performance, we conduct experiments with ranks of 4, 8, 16, and 32, with the results detailed in Tab. 5. As shown in the table, the model’s performance varies with different ranks, achieving optimal results when the LoRA rank is set to 8.

**Effects of Joint Training Datasets.** To validate the effects of joint training with multiple datasets, we design a progressive experimental setup, with results presented in Tab. 6. In this study, A, B, C, and D represent the WHU-CD,

Table 4. Effects of different vision backbone.

Vision Backbone	SECOND		S2Looking	
	SeK	mIoU	F1	IoU
SAM [25]	14.63	67.78	59.51	42.36
SAM2 [35]	13.84	67.48	59.13	41.97
RSBuilding-ViT-L [40]	19.30	71.11	66.76	50.10
SAM(ft)	22.50	72.53	66.87	50.23
SAM2(ft)	22.82	72.63	67.42	50.85
RSBuilding-ViT-L(ft)	<b>23.02</b>	<b>72.85</b>	<b>69.32</b>	<b>53.04</b>

Table 5. Effects of different lora rank.

Lora Rank	WHU-CD		S2Looking	
	F1	IoU	F1	IoU
4	94.68	89.89	68.53	52.13
8	<b>94.96</b>	<b>90.41</b>	<b>69.32</b>	<b>53.04</b>
16	94.82	90.15	68.42	52.00
32	94.81	90.13	68.16	51.70

Table 6. Effects of joint training datasets. A, B, C, and D represent the WHU-CD, S2Looking, LEVIR-CD+, and SECOND datasets.

Training Dataset	A	B	C	D	
	IoU	IoU	IoU	mIoU	SeK
✓ - - -	89.68	-	-	-	-
✓ ✓ - -	89.77	52.57	-	-	-
✓ ✓ ✓ -	90.16	52.51	78.43	-	-
✓ ✓ ✓ ✓	<b>90.41</b>	<b>53.04</b>	<b>78.87</b>	<b>72.85</b>	<b>23.02</b>

S2Looking, LEVIR-CD+, and SECOND datasets, respectively. We progressively increase the number of datasets in the training mixture, starting with only A, then A+B, followed by A+B+C, and finally A+B+C+D. A trend emerges from the results: as more datasets are added to the training mixture, the model’s overall performance shows an upward trend. This indicates that joint training allows the model to learn more general and robust representations, leading to improved overall performance. The best results for all datasets are achieved when the model is trained jointly on all four datasets.

## 4.6. Visualisation Results

As illustrated in Fig. 4, we present the visualisation results for UniChange. It can be observed that UniChange demonstrates commendable performance across both BCD and SCD tasks.

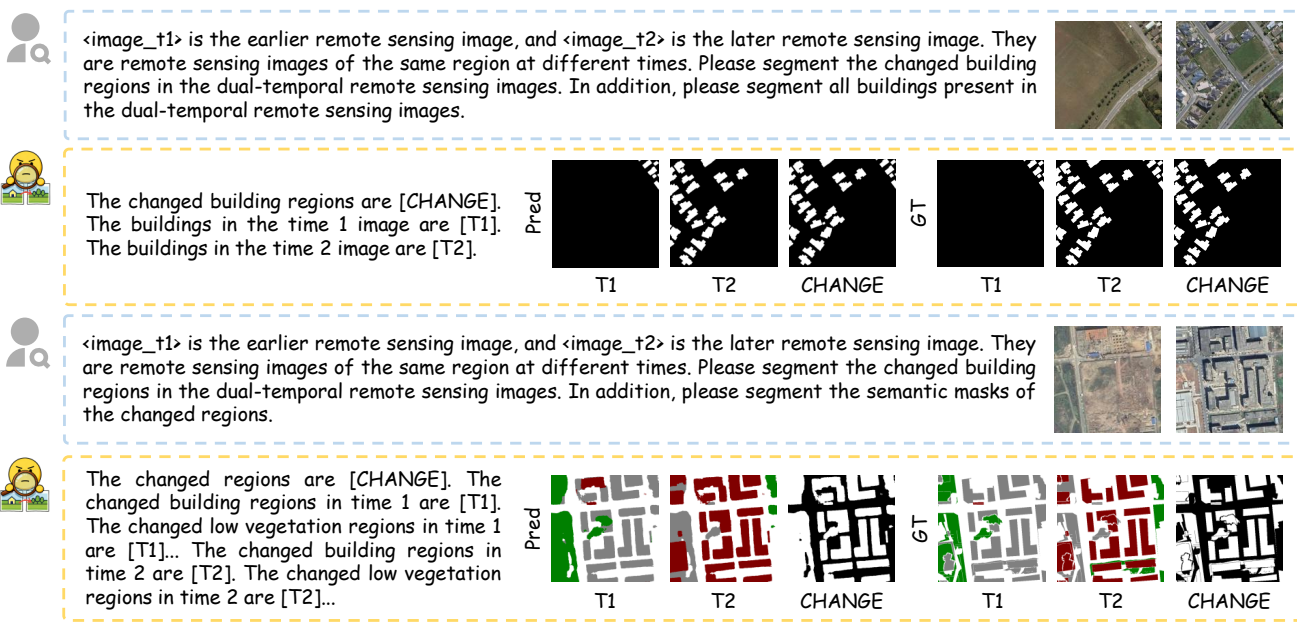


Figure 4. Visualisation results from UniChange. The images for the first question are sourced from the binary change detection dataset WHU-CD. The images for the second question are sourced from the semantic change detection dataset SECONd.

## 5. Conclusion

In this paper, we introduce UniChange, the first unified change detection framework built upon MLLM. This framework addresses the fundamental challenges of task fragmentation and dataset incompatibility that constrain conventional change detection models. Our approach reframes both BCD task and SCD task as instruction-guided grounding tasks. By utilizing three special tokens: [T1], [T2], and [CHANGE] and leveraging text prompts for classification, UniChange eliminates the reliance on predefined classification heads. This design uniquely allows the model to acquire comprehensive knowledge by jointly training on diverse, multi-source datasets, even when their semantic labels conflict. Our approach achieves state-of-the-art performance on four public benchmarks (WHU-CD, S2Looking, LEVIR-CD+, and SECONd), demonstrating its superiority.

## References

- [1] Saeid Asadzadeh, Wilson José de Oliveira, and Carlos Roberto de Souza Filho. Uav-based remote sensing for the petroleum industry and environmental monitoring: State-of-the-art and perspectives. *Journal of Petroleum Science and Engineering*, 208:109633, 2022. 1
- [2] Wele Gedara Chaminda Bandara and Vishal M Patel. A transformer-based siamese network for change detection. In *IGARSS 2022-2022 IEEE International Geoscience and Remote Sensing Symposium*, pages 207–210. IEEE, 2022. 2, 3, 7
- [3] Hao Chen and Zhenwei Shi. A spatial-temporal attention-based method and a new dataset for remote sensing image change detection. *Remote sensing*, 12(10):1662, 2020. 6
- [4] Hao Chen, Zipeng Qi, and Zhenwei Shi. Remote sensing image change detection with transformers. *IEEE Transactions on Geoscience and Remote Sensing*, 60:1–14, 2021. 2, 3, 7
- [5] Jie Chen, Ziyang Yuan, Jian Peng, Li Chen, Haozhe Huang, Jiawei Zhu, Yu Liu, and Haifeng Li. Dasnet: Dual attentive fully convolutional siamese networks for change detection in high-resolution satellite images. *IEEE Journal of Selected Topics in Applied Earth Observations and Remote Sensing*, 14:1194–1206, 2020. 7
- [6] Keyan Chen, Chengyang Liu, Wenyuan Li, Zili Liu, Hao Chen, Haotian Zhang, Zhengxia Zou, and Zhenwei Shi. Time travelling pixels: Bitemporal features integration with foundation model for remote sensing image change detection. In *IGARSS 2024-2024 IEEE International Geoscience and Remote Sensing Symposium*, pages 8581–8584. IEEE, 2024. 7
- [7] Fengzhi Cui and Jie Jiang. Mtscd-net: A network based on multi-task learning for semantic change detection of bitemporal remote sensing images. *International Journal of Applied Earth Observation and Geoinformation*, 118:103294, 2023. 2, 3, 7
- [8] Wenliang Dai, Junnan Li, Dongxu Li, Anthony Tiong, Junqi Zhao, Weisheng Wang, Boyang Li, Pascale N Fung, and Steven Hoi. Instructblip: Towards general-purpose vision-language models with instruction tuning. *Advances in neural information processing systems*, 36:49250–49267, 2023. 3
- [9] Rodrigo Caye Daudt, Bertrand Le Saux, and Alexandre Boulch. Fully convolutional siamese networks for change detection. In *2018 25th IEEE international conference on image processing (ICIP)*, pages 4063–4067. IEEE, 2018. 1, 3, 7

[10] Rodrigo Caye Daudt, Bertrand Le Saux, Alexandre Boulch, and Yann Gousseau. Multitask learning for large-scale semantic change detection. *Computer Vision and Image Understanding*, 187:102783, 2019. [2](#), [3](#)

[11] Lei Ding, Haitao Guo, Sicong Liu, Lichao Mou, Jing Zhang, and Lorenzo Bruzzone. Bi-temporal semantic reasoning for the semantic change detection in hr remote sensing images. *IEEE Transactions on Geoscience and Remote Sensing*, 60: 1–14, 2022. [2](#), [3](#), [7](#)

[12] Lei Ding, Kun Zhu, Daifeng Peng, Hao Tang, Kuiwu Yang, and Lorenzo Bruzzone. Adapting segment anything model for change detection in vhr remote sensing images. *IEEE Transactions on Geoscience and Remote Sensing*, 62:1–11, 2024. [2](#), [3](#), [7](#)

[13] Qing Ding, Zhenfeng Shao, Xiao Huang, Fengyan Wang, and Mingchang Wang. Mlfa-net: multi-level feature-aggregated network for semantic change detection in remote sensing images. *International Journal of Digital Earth*, 17(1):2398070, 2024. [7](#)

[14] Sijun Dong, Libo Wang, Bo Du, and Xiaoliang Meng. Changeclip: Remote sensing change detection with multi-modal vision-language representation learning. *ISPRS Journal of Photogrammetry and Remote Sensing*, 208:53–69, 2024. [7](#)

[15] Sheng Fang, Kaiyu Li, Jinyuan Shao, and Zhe Li. Snunet-cd: A densely connected siamese network for change detection of vhr images. *IEEE Geoscience and Remote Sensing Letters*, 19:1–5, 2021. [7](#)

[16] Sheng Fang, Kaiyu Li, and Zhe Li. Changer: Feature interaction is what you need for change detection. *IEEE Transactions on Geoscience and Remote Sensing*, 61:1–11, 2023. [2](#), [3](#)

[17] Yuchao Feng, Jiawei Jiang, Honghui Xu, and Jianwei Zheng. Change detection on remote sensing images using dual-branch multilevel intertemporal network. *IEEE Transactions on Geoscience and Remote Sensing*, 61:1–15, 2023. [2](#), [3](#)

[18] Yuhang Gan, Wenjie Xuan, Hang Chen, Juhua Liu, and Bo Du. Rfl-cdnet: Towards accurate change detection via richer feature learning. *Pattern Recognition*, 153:110515, 2024. [7](#)

[19] Yuhang Gan, Wenjie Xuan, Zhiming Luo, Lei Fang, Zeng-mao Wang, Juhua Liu, and Bo Du. Detect changes like humans: Incorporating semantic priors for improved change detection. *IEEE Transactions on Geoscience and Remote Sensing*, 2025. [7](#)

[20] Junyu Gao, Da Zhang, Feiyu Wang, Lichen Ning, Zhiyuan Zhao, and Xuelong Li. Combining sam with limited data for change detection in remote sensing. *IEEE Transactions on Geoscience and Remote Sensing*, 2025. [7](#)

[21] Haonan Guo, Xin Su, Chen Wu, Bo Du, and Liangpei Zhang. Saan: Similarity-aware attention flow network for change detection with vhr remote sensing images. *IEEE Transactions on Image Processing*, 33:2599–2613, 2024. [7](#)

[22] Edward J Hu, Yelong Shen, Phillip Wallis, Zeyuan Allen-Zhu, Yuanzhi Li, Shean Wang, Lu Wang, Weizhu Chen, et al. Lora: Low-rank adaptation of large language models. *ICLR*, 1(2):3, 2022. [4](#)

[23] Yuan Hu, Jianlong Yuan, Congcong Wen, Xiaonan Lu, Yu Liu, and Xiang Li. Rsgpt: A remote sensing vision language model and benchmark. *ISPRS Journal of Photogrammetry and Remote Sensing*, 224:272–286, 2025. [3](#)

[24] Shunping Ji, Shiqing Wei, and Meng Lu. Fully convolutional networks for multisource building extraction from an open aerial and satellite imagery data set. *IEEE Transactions on Geoscience and Remote Sensing*, 57(1):574–586, 2019. [6](#)

[25] Alexander Kirillov, Eric Mintun, Nikhila Ravi, Hanzi Mao, Chloe Rolland, Laura Gustafson, Tete Xiao, Spencer Whitehead, Alexander C Berg, Wan-Yen Lo, et al. Segment anything. In *Proceedings of the IEEE/CVF international conference on computer vision*, pages 4015–4026, 2023. [2](#), [3](#), [8](#)

[26] Kartik Kuckreja, Muhammad S Danish, Muzammal Naseer, Abhijit Das, Salman Khan, and Fahad S Khan. Geochat: Grounded large vision-language model for remote sensing. the ieee. In *CVF Conference on Computer Vision and Pattern Recognition*, page 4, 2024. [3](#)

[27] Xin Lai, Zhuotao Tian, Yukang Chen, Yanwei Li, Yuhui Yuan, Shu Liu, and Jiaya Jia. Lisa: Reasoning segmentation via large language model. In *Proceedings of the IEEE/CVF Conference on Computer Vision and Pattern Recognition*, pages 9579–9589, 2024. [3](#)

[28] Yuxuan Li, Yicheng Zhang, Wenhao Tang, Yimian Dai, Ming-Ming Cheng, Xiang Li, and Jian Yang. Visual instruction pretraining for domain-specific foundation models. *arXiv preprint arXiv:2509.17562*, 2025. [3](#)

[29] Haotian Liu, Chunyuan Li, Qingyang Wu, and Yong Jae Lee. Visual instruction tuning. *Advances in neural information processing systems*, 36:34892–34916, 2023. [3](#), [5](#)

[30] Ilya Loshchilov and Frank Hutter. Decoupled weight decay regularization. *arXiv preprint arXiv:1711.05101*, 2017. [6](#)

[31] Liye Mei, Zhaoyi Ye, Chuan Xu, Hongzhu Wang, Ying Wang, Cheng Lei, Wei Yang, and Yansheng Li. Scd-sam: Adapting segment anything model for semantic change detection in remote sensing imagery. *IEEE Transactions on Geoscience and Remote Sensing*, 62:1–13, 2024. [1](#), [2](#), [3](#), [7](#)

[32] Daifeng Peng, Lorenzo Bruzzone, Yongjun Zhang, Haiyan Guan, and Pengfei He. Scdnet: A novel convolutional network for semantic change detection in high resolution optical remote sensing imagery. *International Journal of Applied Earth Observation and Geoinformation*, 103:102465, 2021. [3](#), [7](#)

[33] Zhiliang Peng, Wenhui Wang, Li Dong, Yaru Hao, Shaohan Huang, Shuming Ma, Qixiang Ye, and Furu Wei. Grounding multimodal large language models to the world. In *The Twelfth International Conference on Learning Representations*, 2024. [3](#)

[34] Jeff Rasley, Samyam Rajbhandari, Olatunji Ruwase, and Yuxiong He. Deepspeed: System optimizations enable training deep learning models with over 100 billion parameters. In *Proceedings of the 26th ACM SIGKDD international conference on knowledge discovery & data mining*, pages 3505–3506, 2020. [5](#)

[35] Nikhila Ravi, Valentin Gabeur, Yuan-Ting Hu, Ronghang Hu, Chaitanya Ryali, Tengyu Ma, Haitham Khedr, Roman Rädle, Chloe Rolland, Laura Gustafson, et al. Sam 2: Segment anything in images and videos. *arXiv preprint arXiv:2408.00714*, 2024. [2](#), [3](#), [8](#)

[36] Akashah Shabbir, Mohammed Zumri, Mohammed Ben-namoun, Fahad S Khan, and Salman Khan. Geopixel: Pixel grounding large multimodal model in remote sensing. *arXiv preprint arXiv:2501.13925*, 2025. 3

[37] Li Shen, Yao Lu, Hao Chen, Hao Wei, Donghai Xie, Jiabao Yue, Rui Chen, Shouye Lv, and Bitao Jiang. S2looking: A satellite side-looking dataset for building change detection. *Remote Sensing*, 13(24):5094, 2021. 6

[38] Ashbindu Singh. Change detection in the tropical forest environment of northeastern india using landsat. *Remote sensing and tropical land management*, 44:273–254, 1986. 1

[39] Biao Wang, Zhenghao Jiang, Weichun Ma, Xiao Xu, Peng Zhang, Yanlan Wu, and Hui Yang. Dual-dimension feature interaction for semantic change detection in remote sensing images. *IEEE Journal of Selected Topics in Applied Earth Observations and Remote Sensing*, 17:9595–9605, 2024. 7

[40] Mingze Wang, Lili Su, Cilin Yan, Sheng Xu, Pengcheng Yuan, Xiaolong Jiang, and Baochang Zhang. Rsbuiding: Towards general remote sensing image building extraction and change detection with foundation model. *IEEE Transactions on Geoscience and Remote Sensing*, 2024. 2, 3, 5, 8

[41] Thilo Wellmann, Angela Lausch, Erik Andersson, Sonja Knapp, Chiara Cortinovis, Jessica Jache, Sebastian Scheuer, Peleg Kremer, André Mascarenhas, Roland Kraemer, et al. Remote sensing in urban planning: Contributions towards ecologically sound policies? *Landscape and urban planning*, 204:103921, 2020. 1

[42] Ge Wu, Shen Zhang, Ruijing Shi, Shanghua Gao, Zhenyuan Chen, Lei Wang, Zhaowei Chen, Hongcheng Gao, Yao Tang, Jian Yang, et al. Representation entanglement for generation: Training diffusion transformers is much easier than you think. *arXiv preprint arXiv:2507.01467*, 2025. 3

[43] Chuan Xu, Zhaoyi Ye, Liye Mei, Haonan Yu, Jianchen Liu, Yaxiaer Yalikun, Shuangtong Jin, Sheng Liu, Wei Yang, and Cheng Lei. Hybrid attention-aware transformer network collaborative multiscale feature alignment for building change detection. *IEEE Transactions on Instrumentation and Measurement*, 73:1–14, 2024. 2, 3

[44] Kunping Yang, Gui-Song Xia, Zicheng Liu, Bo Du, Wen Yang, Marcello Pelillo, and Liangpei Zhang. Asymmetric siamese networks for semantic change detection in aerial images. *IEEE Transactions on Geoscience and Remote Sensing*, 60:3113912, 2022. 6

[45] Haoxuan You, Haotian Zhang, Zhe Gan, Xianzhi Du, Bowen Zhang, Zirui Wang, Liangliang Cao, Shih-Fu Chang, and Yinfei Yang. Ferret: Refer and ground anything anywhere at any granularity. *arXiv preprint arXiv:2310.07704*, 2023. 3

[46] Chenxiao Zhang, Peng Yue, Deodato Tapete, Liangcun Jiang, Boyi Shangguan, Li Huang, and Guangchao Liu. A deeply supervised image fusion network for change detection in high resolution bi-temporal remote sensing images. *ISPRS Journal of Photogrammetry and Remote Sensing*, 166:183–200, 2020. 2, 3

[47] Cui Zhang, Liejun Wang, Shuli Cheng, and Yongming Li. Swinsunet: Pure transformer network for remote sensing im- age change detection. *IEEE Transactions on Geoscience and Remote Sensing*, 60:1–13, 2022. 2, 3

[48] Da Zhang, Feiyu Wang, Lichen Ning, Zhiyuan Zhao, Junyu Gao, and Xuelong Li. Integrating sam with feature interaction for remote sensing change detection. *IEEE Transactions on Geoscience and Remote Sensing*, 2024. 7

[49] Shilong Zhang, Peize Sun, Shoufa Chen, Min Xiao, Wenqi Shao, Wenwei Zhang, Yu Liu, Kai Chen, and Ping Luo. Gpt4roi: Instruction tuning large language model on region-of-interest. In *European conference on computer vision*, pages 52–70. Springer, 2024. 3

[50] Xu Zhao, Wenchao Ding, Yongqi An, Yinglong Du, Tao Yu, Min Li, Ming Tang, and Jinqiao Wang. Fast segment anything. *arXiv preprint arXiv:2306.12156*, 2023. 2, 3

[51] Zhuo Zheng, Yanfei Zhong, Junjue Wang, Ailong Ma, and Liangpei Zhang. Building damage assessment for rapid disaster response with a deep object-based semantic change detection framework: From natural disasters to man-made disasters. *Remote Sensing of Environment*, 265:112636, 2021. 1

[52] Zhuo Zheng, Yanfei Zhong, Shiqi Tian, Ailong Ma, and Liangpei Zhang. Changemask: Deep multi-task encoder-transformer-decoder architecture for semantic change detection. *ISPRS Journal of Photogrammetry and Remote Sensing*, 183:228–239, 2022. 7

[53] Deyao Zhu, Jun Chen, Xiaoqian Shen, Xiang Li, and Mohamed Elhoseiny. Minigpt-4: Enhancing vision-language understanding with advanced large language models. *arXiv preprint arXiv:2304.10592*, 2023. 3